nature electronics

Article

https://doi.org/10.1038/s41928-024-01303-z

Neuromorphic weighted sums with magnetic skyrmions

Received: 31 October 2023

Accepted: 5 November 2024

Published online: 06 January 2025

Check for updates

Tristan da Câmara Santa Clara Gomes[1,2] ✉, Yanis Sassi[1], Dédalo Sanz-Hernández[1], Sachin Krishnia[1], Sophie Collin[1], Marie-Blandine Martin[1], Pierre Seneor[1], Vincent Cros[1] ✉, Julie Grollier[1] ✉ & Nicolas Reyren[1] ✉

Integrating magnetic skyrmions into neuromorphic computing could help improve hardware efficiency and computational power. However, developing a scalable implementation of the weighted sum of neuron signals—a core operation in neural networks—has remained a challenge. Here we show that weighted sum operations can be performed in a compact, biologically inspired manner by using the non-volatile and particle-like characteristics of magnetic skyrmions that make them easily countable and summable. The skyrmions are electrically generated in numbers proportional to an input with an efficiency given by a non-volatile weight. The chiral particles are then directed using localized current injections to a location in which their presence is quantified through non-perturbative electrical measurements. Our experimental demonstration, which currently has two inputs, can be scaled to accommodate multiple inputs and outputs using a crossbar-array design, potentially nearing the energy efficiency observed in biological systems.

Magnetic skyrmions are topological magnetic solitons behaving like particles. They are stabilized at room temperature in magnetic thin films or heterostructures with optimized magnetic anisotropy and Dzyaloshinskii–Moriya interaction[1–5]. Recent experimental studies have shown that magnetic skyrmions can be nucleated[3,6–10], moved[3,4,6], annihilated[11,12] and electrically detected using the anomalous Hall effect (AHE)[13,14] or tunnel magnetoresistance (TMR)[15–17].

Magnetic skyrmions have a range of features that make them suitable for energy-efficient computing operations[1,18,19], such as stability at room temperature, deep submicrometre dimensions, non-volatility, particle-like behaviour and motion at low power. These characteristics align closely with the needs of neuromorphic computing[20], and recent reports have shown that skyrmions can provide various roles in neuromorphic circuits, from acting as artificial synapses[19,21] and neurons[20,22,23] to functioning as stochastic reshufflers[24,25]. They can even facilitate reservoir computing for data classification based on particle dynamics[18,26–29]. However, a fundamental neural network operation—the weighted sum of input neuron signals—is still missing in the context of skyrmions[20].

A weighted sum operation involves multiplying each input X_i (where i relates to the index) by a tunable factor known as the synaptic weight w_i (Fig. 1a). The subsequent results Y_i are then summed to produce the final outcome $Y_{\mathrm{tot}} = \sum_{i=1}^{M} Y_i = \sum_{i=1}^{M} w_i X_i$, where M is the number of inputs. Complementary metal–oxide–semiconductor (CMOS) neuromorphic circuits achieve weighted sums through the combined use of transistors and static random-access memories that have a large silicon footprint (several square micrometres per synapse), volatile weights and consume tens of picojoules per synaptic operation[30]. Biological systems, by contrast, achieve the weighted sum through the nucleation and release of vesicles under electrical stimulation, followed by the accumulation and detection of neurotransmitters that they contain to produce the output spikes (Fig. 1b). They are extremely efficient with non-volatile synapses of submicrometre dimensions, and an energy cost of approximately 25 fJ per synaptic event corresponding mainly to vesicle release[31,32].

In this Article, we report an experimental demonstration of a neuromorphic weighted sum with magnetic skyrmions (Fig. 1c).

[1]Laboratoire Albert Fert, CNRS, Thales, Université Paris-Saclay, Palaiseau, France. [2]Present address: Institute of Condensed Matter and Nanosciences, Université Catholique de Louvain, Louvain-la-Neuve, Belgium. ✉e-mail: tristan.dacamara@uclouvain.be; vincent.cros@cnrs-thales.fr; julie.grollier@cnrs-thales.fr; nicolas.reyren@cnrs-thales.fr

https://doi.org/10.1038/s41928-024-01303-z

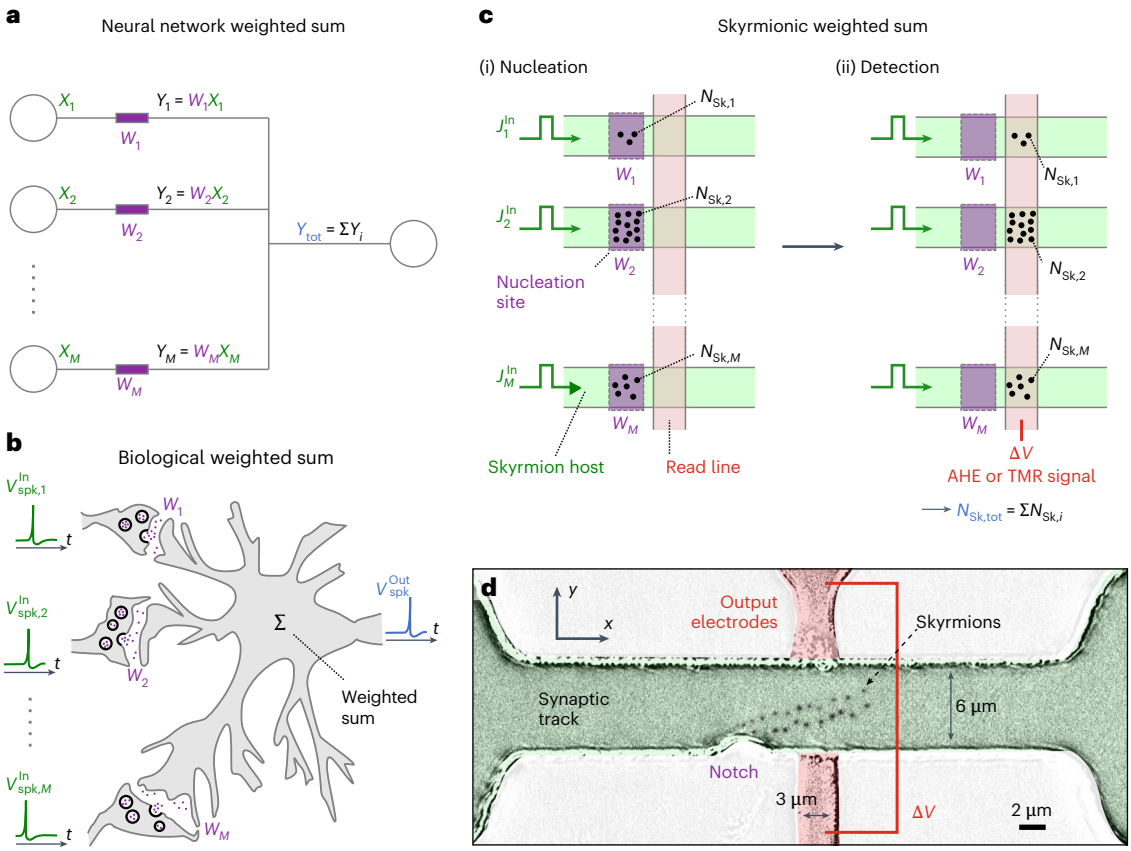

Fig. 1 | Skyrmionic weighted sum building blocks. a, Working principle of a neural network weighted sum that emulates the functionality of the biological neural network. The input values X_i are multiplied by their respective synaptic weights w_i to generate Y_i values that can be summed to produce an output $Y_{tot} = \sum_i Y_i$. **b**, Illustration of a biological weighted summation operation within a neuron. The neuron receives spike voltage signals $V^{In}_{spk,i}$ at various times through synapses, each with its associated synaptic weight w_i. This induces the nucleation and motion of vesicles (black circles) containing neurotransmitters (violet dots). These neurotransmitters accumulate at the neuron receptors, resulting in the weighted summation operation $\sum_i w_i V^{In}_{spk,i}$. The neuron generates an output spike V^{Out}_{spk} when this summation reaches a threshold value, thereby implementing the nonlinear activation function. **c**, Schematic of our implementation of a skyrmionic weighted sum, which performs the necessary operation for a neural network weighted sum. Electrical inputs J^{In}_i are applied to skyrmion host tracks (in green) to nucleate the controlled number of magnetic skyrmions $N_{Sk,i}$ at the nucleation sites, each with an assigned synaptic weight w_i so that $N_{Sk,i} = w_i J^{In}_i$. These skyrmions are moved into a transverse electrical detection zone, established by the intersection of the track and read line for the electrical output (in red), where the cumulative number of skyrmions $N_{Sk,tot} = \sum_i N_{Sk,i}$ can be electrically detected through an output voltage ΔV arising from the AHE or TMR. **d**, Kerr microscopy difference image of the device with magnetic skyrmions (dark spots), which were nucleated from a notch in a 6-µm-wide synaptic track made of a Ta(5 nm)/Pt(8 nm)/[Co(1.2 nm)/Al(3 nm)/Pt(3 nm)]$_{10}$ multilayer. Skyrmions moved between the detection electrodes made of 3-µm-wide and 10-nm-thick Ta electrodes connected only at the edges of the track.

When an electrical current pulse is injected along a track with index i, a corresponding number of skyrmions $N_{Sk,i}$ is produced in the nucleation zone. The intention is for this number to be proportional to the input values—signified by the current pulse in each track J^{In}_i—multiplied by a factor w_i, which represents the weights of the weighted sum: $N_{Sk,i} = w_i J^{In}_i$. These skyrmions, once generated, can be displaced under the action of electrical pulses of smaller amplitude through the action of spin–orbit torques (SOT) to accumulate in a specific region, enabling a spatial summation expressed as $N_{Sk,tot} = \sum_i N_{Sk,i}$. The total number of skyrmions in a selected region can be detected using magnetoresistive means[13,14,16,17] and can, therefore, implement the weighted sum of inputs:

$$N_{Sk,tot} = \sum_i w_i J^{In}_i \quad . \tag{1}$$

We show that this approach allows for an electrical readout of the total sum. We exploit the unique quasiparticle and non-volatility properties of skyrmions, making them easily countable and summable, and use these properties to perform the weighted sum operation over the number of skyrmions. In this approach, the skyrmions are nucleated and moved in a manner reminiscent of vesicles, and detected and accumulated within neurons in a way analogous to neurotransmitters (Fig. 1)[33]. A similar functionality could also be achieved with other particle-like magnetic textures like hopfions[34] or skyrmionic cocoons[35], although their electrical control is currently less advanced.

We show that electrical pulses can nucleate a controllable number of skyrmions from a notch in the host material at room temperature (Fig. 1d). The number of generated skyrmions directly correlates with the count of applied electrical pulses, allowing efficient input encoding (equation (1)). The weight factor, influenced by the notch's geometry, can be adjusted by changing the magnetic field applied on the structure (but more practical non-volatile solutions exist). We then non-perturbatively detect the nucleated skyrmions using the AHE. Finally, we showcase an experimental demonstration of the weighted sum with a two-input-to-one-output configuration. Our skyrmionic weighted sum approach offers non-volatile weights and compactness due to fully electrical, local operations at a submicrometre scale. We show that the concept is scalable to multiple inputs and outputs by

using a crossbar-array-like geometry, with the potential of reaching the energy efficiency found in biological systems.

Electric-pulse-controlled nucleation and motion of skyrmions

The first experimental challenge to realize the weighted sum is to achieve a precise control of skyrmions nucleation: the quantity of nucleated skyrmions should be directly proportional to the input. This necessitates the development of a reliable method to encode this input within the current pulses that drive the nucleation. Furthermore, the proportionality factor, representing the weight, should be adjustable to enable learning. The second challenge involves ensuring that all the nucleated skyrmions are reliably transported from their nucleation site to the designated accumulation and detection region without the loss or gain of skyrmions. The incorporation of detection circuits (Fig. 1c,d, red area) can lead to localized alterations in current density, which can impact the motion of skyrmions. In particular, the Hall cross geometry, which is frequently used for skyrmion detection, can hinder the movement of some or all the skyrmions due to reduced current density at its centre.

Our building block is shown in Fig. 1d (Methods provides more details). The multilayer track is optimized to stabilize the isolated skyrmions of approximately 200 nm in diameter at room temperature and to facilitate efficient current-driven skyrmion motion by SOT[36]. The skyrmion nucleation site is implemented by a notch that enables a local increase in current density, surpassing the threshold for skyrmion nucleation, and ensuring the rest of the track remains below this threshold[6] (Supplementary Note 1). Skyrmion detection is performed through AHE using a specially crafted Hall cross geometry. We design tantalum (Ta)-based Hall electrodes that are two orders of magnitude more resistive than the skyrmion track, connected solely to their edge to minimize spatial variations of the current density and eliminate potential current leaks that might disrupt skyrmion movement (Supplementary Note 1).

The controlled generation of skyrmions by current injection in our building block device is demonstrated in Fig. 2. As a preparatory step, we orient the magnetization vertically (along the $+z$ direction) by applying an out-of-plane (OOP) magnetic field of 200 mT, ensuring complete saturation of magnetization. Subsequently, by injecting current pulses (current density, $J = 160$ GA m^{-2}; pulse duration, $t = 50$ ns) under an OOP magnetic field ($\mu_0 H_z = 24$ mT), we selectively nucleate magnetic skyrmions at the notch. Following their formation, these skyrmions are transported, driven by the SOT mechanism[3,4,6], to the designated detection region.

The skyrmion count within the track increases linearly with the number of applied current pulses (Fig. 2a,d). The skyrmions, being nucleated sequentially, form a linear arrangement, following a characteristic oblique trajectory, which is attributed to the inherent topological properties of the skyrmions—the skyrmion Hall effect[37]. The skyrmion Hall angle, which quantifies the deviation between the current's direction (along x) and the skyrmion's propagation path, is approximately 15°, consistent with the anticipated angle for this specific material system at the experimental current density[6].

To mitigate any potential adverse effects from such transversal motion, the Hall electrodes are positioned close to the notch. This ensures that skyrmions are detected before approaching the track's opposite edge (Fig. 2a–d). As expected from the skyrmion Hall angle, we determine that skyrmions typically cover a distance of ~15 µm longitudinally (in the x direction) before nearing the opposing boundary of the track. By analysing the skyrmion velocity as a function of the position in the track, we observe that the train of skyrmions can completely cross the area of the Ta-based electrodes without any detectable reduction in their velocity and perturbation of their trajectory, because of the much larger sheet resistance of the Ta layer compared with the magnetic multilayer (Supplementary Notes 1 and 2). These findings represent a critical advancement in the design of anomalous Hall detection, with important implications for skyrmion racetrack memories[38,39], where the perturbation of the skyrmion motion at the detection electrodes can affect the functioning of the device. In the present device, we find a skyrmion velocity ranging from a few metres per second to a few tens of metres per second for current densities ranging from 150 GA m^{-2} to 200 GA m^{-2}. The relation between the number of nucleated skyrmions per pulse and the current density displays a quadratic behaviour, which is the signature of a thermally driven skyrmion nucleation process (Supplementary Note 3).

Transformation of electrical pulse inputs into skyrmion numbers

We demonstrate that our device design enables controlled skyrmion generation, with a linear evolution of their number with the input required to implement the weighted sum operation (equation (1)). In Fig. 2e,f, we display the evolution of the number of nucleated skyrmions N_{Sk} in the track observed by Kerr microscopy as a function of the number of current pulses injected in the track, N_{Pulse}, under $\mu_0 H_z = 24$ mT.

Our results, presented for varying J values (Fig. 2e) and different t values (Fig. 2f), consistently show a direct proportionality between the skyrmion count and the number of applied pulses. This underscores our capability to change the number of skyrmions in the track linearly by adjusting the number of input pulses. The nucleation rate of skyrmions per pulse also displays a linear relationship with the pulse duration (Supplementary Note 3 and Supplementary Fig. 4), offering an alternative to the number of current pulses to encode the input.

For specific sets of parameters, for example, $J = 171$ GA m^{-2} and $t = 50$ ns, we observe a one-to-one ratio of skyrmion to pulse (Fig. 2e,f). By modulating these parameters, we can control the nucleation probabilities, thereby achieving a desired skyrmion number in the track. This flexibility allows for either a small number of skyrmions (facilitating optical detection) or a higher number of skyrmions (suitable for more complex operations). The latter is particularly valuable for addressing device sensitivity issues that may arise from small variations in skyrmion numbers or to reduce potential computation errors caused by unintended skyrmion nucleation or annihilation. A high skyrmion count also improves the electrical signal, facilitating electrical detection.

Magnetic-field control of the synaptic weight

In Fig. 2g, we show that the proportionality factor between N_{Sk} and N_{Pulse}, which defines the synaptic weight in our concept, depends on the amplitude of the external perpendicular magnetic field $\mu_0 H_z$. These results demonstrate that the synaptic weight can be tuned by an external OOP magnetic field. The smaller the value of the external magnetic field $\mu_0 H_z$, the larger is the number of nucleated skyrmions for a given current pulse. In particular, more than 50 skyrmions can be nucleated in the 6-µm-wide track in 20 current pulses ($J = 171$ GA m^{-2} and $t = 50$ ns) by decreasing the magnetic field to 20 mT. Depending on the application, the number of states could be adjusted by the skyrmion diameter relative to the track width. Here we focus on accurately assessing the device functionality by quantifying the number of skyrmions through Kerr microscopy. To achieve this, 200-nm-large skyrmions are utilized, alongside a limited number that could be confidently counted visually. However, in practical devices, direct skyrmion observation is unnecessary, allowing for the substantial reduction in skyrmion size down in the range of a few tens of nanometres in diameter and a corresponding increase in their number.

In Fig. 2h, we present the number of skyrmions nucleated per current pulse, or nucleation probability $n_{Sk} = dN_{Sk}/dN_{Pulse}$ extracted from linear fits in Fig. 2g as a function of $\mu_0 H_z$. This nucleation probability is found to decrease linearly with $\mu_0 H_z$. A variation of about −0.57 skyrmions per pulse and per mT is found up to a maximum field of $\mu_0 H_{z,max} = 26$ mT, where no more skyrmions are nucleated (for fixed

https://doi.org/10.1038/s41928-024-01303-z

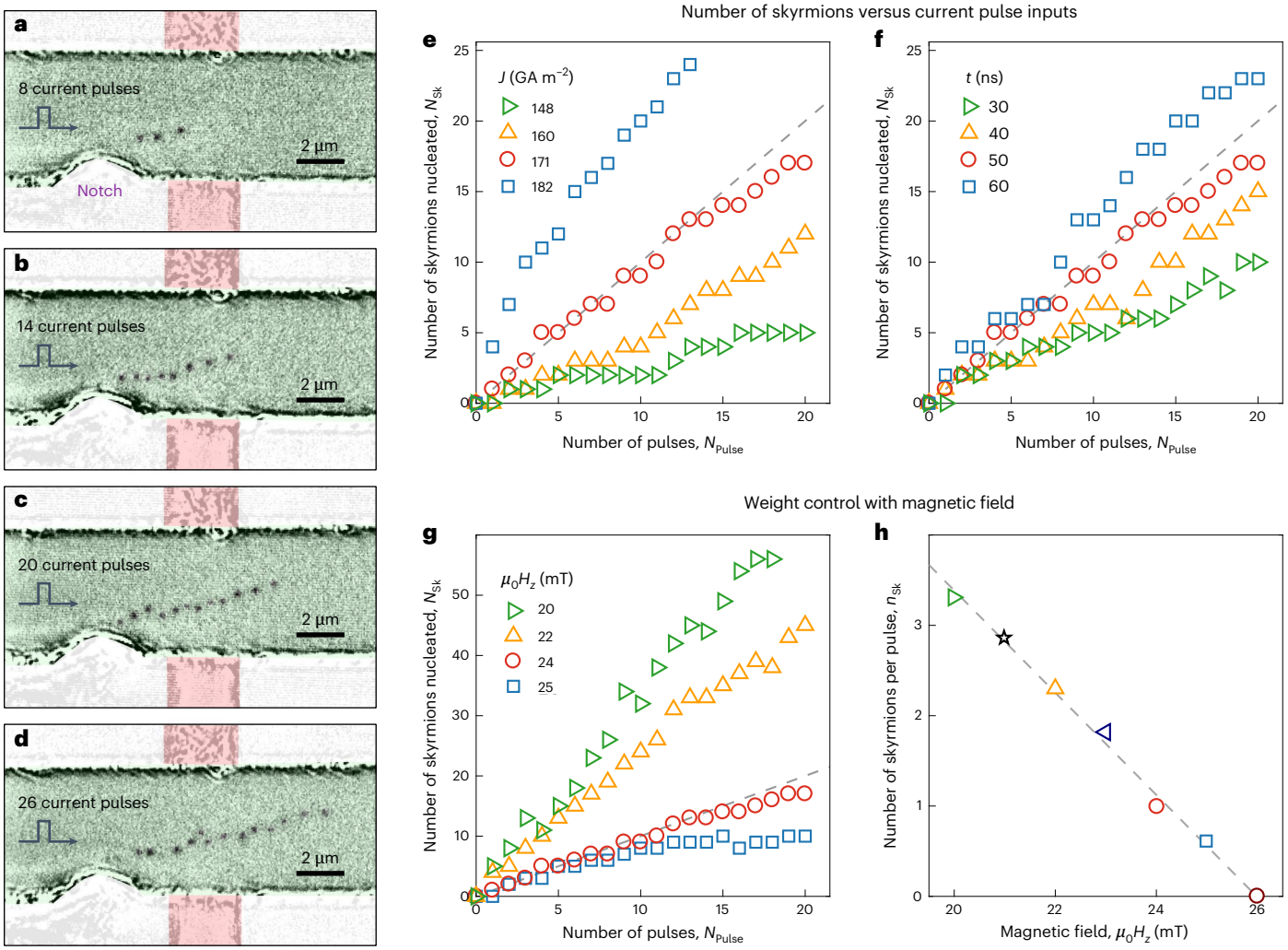

Fig. 2 | Controlled nucleation of magnetic skyrmions at a notch using current pulses as inputs and weight fine-tuning. a–**d**, Kerr microscopy images of the device shown in Fig. 1d, after the application of 8 (**a**), 14 (**b**), 20 (**c**) and 26 (**d**) current pulses at $J = 160$ GA m^{-2}, $t = 50$ ns and $\mu_0 H_z = 24$ mT. **e**,**f**, Number of skyrmions nucleated in the track, N_{Sk}, with the number of pulses applied, N_{Pulse}, (fixed $\mu_0 H_z = 24$ mT) for several current densities J with fixed $t = 50$ ns (**e**) and for several pulse durations t with fixed $J = 171$ GA m^{-2} (**f**). **g**,**h**, Control of weight using the OOP external magnetic fields H_z. **g**, Number of skyrmions nucleated with the number of pulses N_{Pulse} for several OOP external magnetic fields $\mu_0 H_z$ with fixed $J = 171$ GA m^{-2} and $t = 50$ ns. **h**, Linear control of the number of skyrmions nucleated per pulse (slopes in graphs **e**–**g**), n_{Sk}, with $\mu_0 H_z$. The grey dashed lines in **e**–**g** correspond to one nucleated skyrmion per pulse, and in **h**, the grey dashed line is a linear fit with a slope of −0.57 skyrmions per pulse and per mT. The error bars in **h** have a similar magnitude to that of the symbols.

$J = 171$ GA m^{-2} and $t = 50$ ns). On the contrary, if the field is further reduced below 20 mT, elongated domains are found to be nucleated in the track, thereby setting a minimal field for device operation. We estimated the precision on the slope (the synaptic weights) to be approximately 0.1 skyrmions per pulse (Supplementary Note 4). Therefore, this enables the differentiation of 15 synaptic states for field increments of approximately 0.2 mT in our prototype demonstration. This exceeds the six synaptic states achieved with the skyrmion[23], which reached 78% accuracy in recognizing the Modified National Institute of Standards and Technology (MNIST) dataset (with 13 synaptic states reaching a 98.61% accuracy is anticipated, which is nearly equivalent to the ideal full-precision synapse). Increasing the number of skyrmions offers a solution to enhance the weight precision and expand the attainable number of synaptic states. In this context, reducing the skyrmion size allows a larger number of particles, making smaller skyrmions preferable to go towards analogue systems.

Our findings indicate that adjusting the magnetic properties at the nucleation site can effectively modulate the synaptic weight. Importantly, it demonstrates the linearity of the synaptic weight control with the magnetic field. In prospective devices, achieving such modifications could be realized in a non-volatile and local way, possibly leveraging magneto-ionic effects.

Neuronal detection and output

The final summation in our device corresponds in practice to the measurement of the anomalous Hall voltage across the detection area in which skyrmions have been accumulated (Methods, Supplementary Note 2 and Supplementary Fig. 3a,b). The variation in Hall voltage, denoted as ΔV, is shown in Fig. 3 as skyrmions are introduced into the detection zone (Fig. 3, blue dotted square). For the visual detection of skyrmions, we use a 6×6 μm^2 box centred on the Hall bar that is assumed to be the electrical detection area (Supplementary Note 2 and Supplementary Fig. 3). This choice is motivated by a recent study[40], which demonstrated a consistent anomalous Hall voltage contribution for magnetic textures contained within this specific area, whereas the influence of magnetic textures positioned outside this box appears to diminish exponentially as the distance from the Hall cross increases. This variation is shown for three distinct combinations of magnetic

https://doi.org/10.1038/s41928-024-01303-z

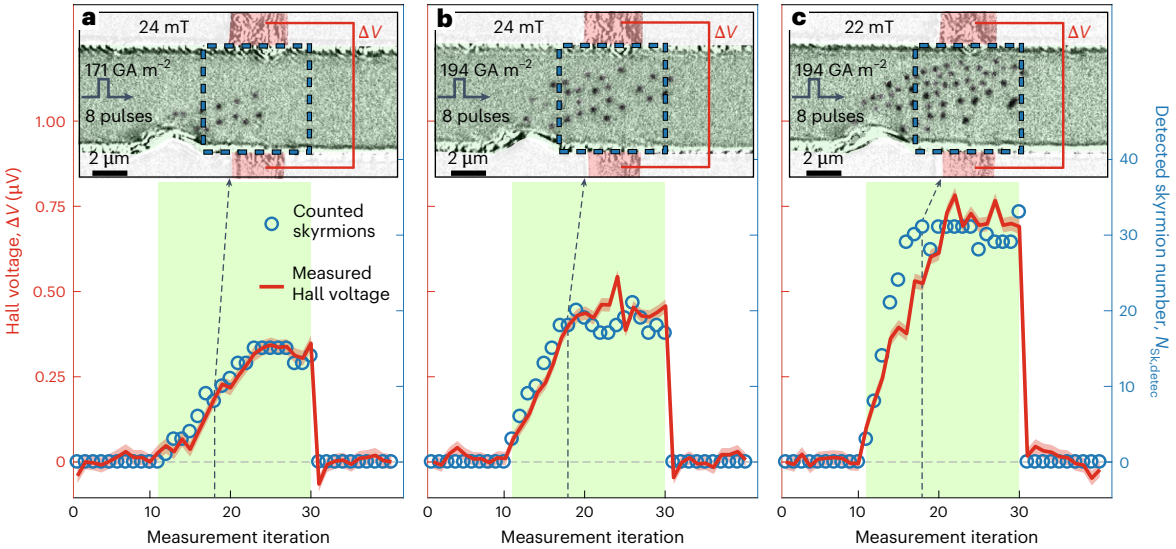

Fig. 3 | Non-perturbative electrical detection of the number of skyrmions using thin Ta electrodes. a–c, Evolution of the Hall voltage $\Delta V = V - V_{sat}$ and the number of detected skyrmions $N_{Sk,detec}$ as a function of the measurement index (one pulse applied before each measurement with indices 11–30) for current pulses with fixed $t = 50$ ns and for $J = 171$ GA m^{-2} (**a**) and $J = 194$ GA m^{-2} (**b** and **c**), and $\mu_0 H_z = 24$ mT (**a** and **b**) and $\mu_0 H_z = 22$ mT (**c**). Ten measurements of voltage are performed before the application of the pulses and after magnetically erasing the skyrmions, defining the saturation voltage V_{sat}. The green-shaded region marks the window in which the current pulses were applied. The insets in **a–c** correspond to the Kerr microscopy images of the nucleated skyrmions after eight current pulses are applied under different conditions (dashed line). The blue dashed boxes indicate the detection zone estimated as a 6-µm-wide square. The red-shaded areas show the uncertainty of the Hall voltage measurements taken as twice the standard deviation of the initial and final 10 measurements (20 measurements in total).

fields and currents. The x axis shows consecutive measurement sequences (Methods). After 10 measurements of the saturated voltage value ($\Delta V \approx 0$), 20 current pulses are used to nucleate the skyrmions (Fig. 3, green area). For each set of conditions, ΔV rises due to the accumulated skyrmions in the detection zone. Then, a saturating field of 200 mT is applied to reset the system (eliminates all the skyrmions), followed by 10 final voltage measurements, which revert to $\Delta V \approx 0$. Reversing the current pulse direction is another way to (electrically) erase skyrmions one by one: the skyrmions move back along the same oblique trajectory and get eventually annihilated at the notch (Supplementary Note 5 and Supplementary Fig. 7). However, this annihilation mechanism can lead to a few residual skyrmions at the notch location, leading to potential small errors in subsequent iterations. The error can be minimized using more pulses, at the expense of a more energetic reset process.

In Fig. 3, each skyrmion contributes equally to reduce the mean magnetization of the initial uniformly magnetized state[13]. This means that the Hall voltage variation ΔV can be directly associated with the number of skyrmions present in the detection zone, denoted as $N_{Sk,detec}$. Alongside the Hall measurements (Fig. 3), we also plot the number of skyrmions identified in the detection zone via Kerr imaging (see the insets). We base our analysis on the assumption that the AHE is proportional to the z component of the magnetization distribution within the 6×6 µm^2 detection area. Skyrmions further away from this centre are excluded from consideration. This methodological choice is supported by experimental data and we show a proportional relationship between ΔV values and the count of skyrmions derived from the magneto-optic Kerr images. In particular, the ratio of the scales on the y axes shown in Fig. 3a–c are constant across all the plots. This showcases the concomitant increase in both skyrmion counts and ΔV values with either increasing pulse current density (Fig. 3a,b) or decreasing $\mu_0 H_z$ (Fig. 3b,c). Given the limited size of the detection zone, both the skyrmion count and the resultant Hall voltage eventually plateau as the detection area becomes saturated or skyrmions begin to move beyond its boundaries.

From our measurements, we find a contribution of approximately 22 nV to the ΔV value for each skyrmion (using a d.c. current of 100 µA) with a standard deviation of 7 nV (Supplementary Note 6). This finding is in line with the data presented elsewhere[13]. Additionally, by analysing the Hall voltage shift during full magnetization reversal of the detection zone (Supplementary Note 2 and Supplementary Fig. 3b) and assuming skyrmions as circular domains with a uniform, opposite 'down' magnetization, we estimate the skyrmion diameter to be approximately 222 ± 33 nm, as expected for such a multilayer track. The estimated standard deviation of the skyrmion diameter primarily arises from uncertainties related to skyrmion counting and electrical noise. Moreover, achieving precise control over the skyrmion diameter is not a fundamental requirement for this study; instead, we focus on harnessing their total number.

Collectively, these results demonstrate the capability of electrically counting skyrmions with high precision using AHE, a crucial aspect for executing the neuromorphic weighted sum operation. The reproducibility of the skyrmion nucleation and Hall voltage output for fixed parameters is demonstrated in Supplementary Note 4.

Demonstration of the weighted sum operation

We present the weighted sum operation using a configuration with two inputs and one output within the device shown in Fig. 4a, consisting of two parallel tracks intersected by a Ta Hall electrode (Methods and Supplementary Note 7). A current pulse generator is connected to track 1 and then to track 2, to successively inject skyrmions in both tracks (Fig. 4b,c), before a reset operation by applying $\mu_0 H_z = 200$ mT (Fig. 4d). The corresponding ΔV for current pulses of about 116 GA m^{-2} and 50 ns with $\mu_0 H_z = 20$ mT is shown in Fig. 4e. The measurement sequence is provided in the Methods. Twenty pulses are applied to track 1, resulting in the concomitant increase in the skyrmion number detected in track 1 via the Hall voltage. The same process is then repeated for track 2, which leads to a further increase in both the total detected skyrmion number and the Hall voltage. The ΔV measured for each successive skyrmion injection agrees with the value expected from individual

https://doi.org/10.1038/s41928-024-01303-z

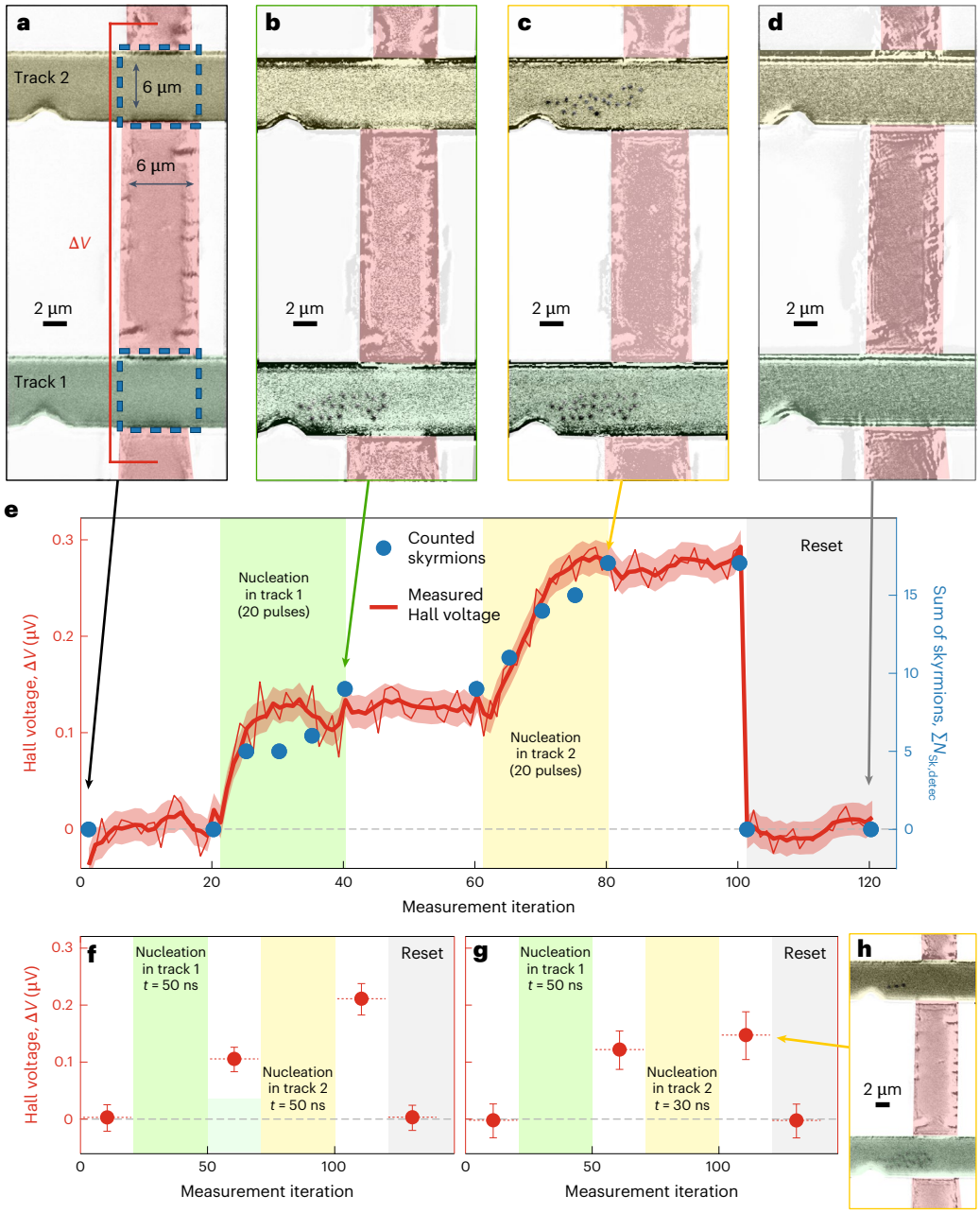

Fig. 4 | Weighted sum in a device composed of two parallel multilayer tracks. **a**–**d**, Kerr microscopy images of the device composed of two 6-µm-wide parallel magnetic multilayer tracks connected by a transverse 6-µm-wide Ta Hall electrode. After the saturation of the track using $\mu_0 H_z = 200$ mT (**a**), skyrmions can be selectively nucleated in track 1 (**b**) and track 2 (**c**), before being erased by another $\mu_0 H_z = 200$ mT (**d**). **e**, ΔV (in red) and the corresponding sum of the skyrmion number detected in both tracks $\sum N_{Sk,detec}$ (in blue) for the successive injection of skyrmions in the tracks. Twenty nucleation pulses are successively applied to each track (green- and yellow-shaded areas for tracks 1 and 2, respectively) using a current pulse of about 116 GA m^{-2} and 50 ns, at $\mu_0 H_z = 20$ mT. The thin (thick) red line shows the raw (smoothened) electrical measurements after drift correction. The red-shaded areas indicate the uncertainty of the Hall voltage measurements taken as twice the standard deviation of the initial and final 20 measurements (40 measurements in total). **f**,**g**, Mean value of ΔV after 30 nucleation pulses successively applied to each track, where the pulse duration applied to track 2 is reduced from 50 ns (**f**) to 30 ns (**g**). **h**, Kerr microscopy images corresponding to the measurement in **g**. The error bars in **f** and **g** represent the standard deviation of the Hall voltage based on 20 specific measurements, with the range of these measurements indicated by the length of the dotted horizontal line.

measurements of the two Hall crosses (Supplementary Note 7 and Supplementary Fig. 10c–j). This result demonstrates that the measured ΔV value is directly proportional to the sum of the skyrmion numbers in the two tracks, as desired for the final sum operation of our device.

This device produces the same weight for each track as the notches are nominally identical, and the external OOP magnetic field is the same over the entire structure. To study the evolution of the AHE voltage for different weights in each track, we can, however, modulate the weight—the number of skyrmions generated by each pulse—by changing the duration of the pulse (Supplementary Note 7 and the linear evolution of the number of skyrmions and the related Hall voltage with pulse duration is shown in Supplementary Fig. 10c–j). In Fig. 4f,g, we illustrate this control, keeping constant the number of current pulses (30), $J = 116$ GA m^{-2} and $\mu_0 H_z = 20$ mT, but varying the pulse duration. In Fig. 4f, the same pulse duration of $t = 50$ ns is used in the two tracks corresponding to identical weights, resulting in two consecutive

https://doi.org/10.1038/s41928-024-01303-z

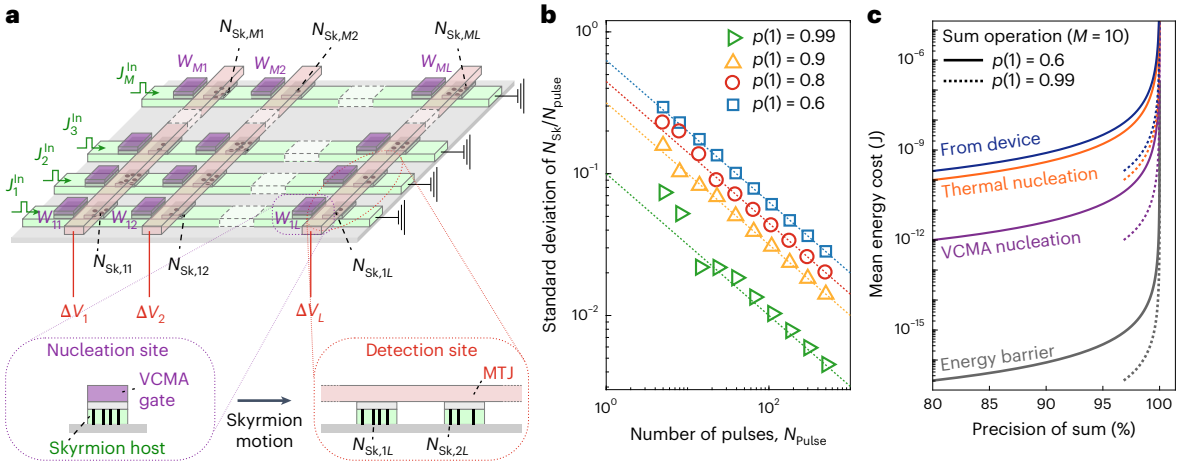

Fig. 5 | Characteristics of a scaled neuromorphic computing device. a, Crossbar architecture comprising M parallel tracks (in green) intersected by L MTJs (red). It enables the introduction of M electrical inputs to inject skyrmions from each nucleation site made of VCMA gates (purple). The skyrmions are then moved into the detection sites where their number naturally sum, inducing L electrical output voltages. The output voltage produced on column j is given by $\Delta V_j = f[\sum_i N_{Sk,ij}] = f[\sum_i (w_{ij} N_{Pulse,i})]$, where i is the track index and f reflects the nonlinear activation function of the MTJ applied to the sum of the skyrmion number $\sum_i N_{Sk,ij}$. **b**, Evolution of the standard deviation σ of N_{Sk} over N_{Pulse} as a function of N_{Pulse} for a single synapse and for several values of the probability of nucleating one skyrmion $p(1)$. The larger the number of attempted skyrmions, or larger the $p(1)$ value, the smaller the relative error, with $\sigma \approx \sqrt{(1-p(1))/N_{Pulse}}$ (represented by the dotted lines for the $p(1)$ values considered). **c**, Estimated mean energy cost in a device composed of ten synapses as a function of the desired weighted sum precision considering the energy to nucleate a single skyrmion as ~20 pJ (estimate from the device shown in Fig. 2), 10 pJ (thermally induced nucleation), 100 fJ (VCMA-induced nucleation) and $500 k_B T \approx 2$ aJ at $T = 300$ K (energy barrier for stable skyrmions).

and identical increases in the Hall voltage, with the mean Hall voltage measuring 105 ± 21 nV and 211 ± 27 nV following nucleation in tracks 1 and 2, respectively. In Fig. 4g, the pulse duration is reduced to $t = 30$ ns for injecting skyrmions in track 2, corresponding to reducing the weight close to zero in this track (Supplementary Note 7 and Supplementary Fig. 10h,j). As expected, the resulting average Hall voltage after the injection in track 2 (147 ± 42 nV) is almost unchanged compared with the value obtained after nucleation in track 1 (121 ± 34 nV). This is equivalent to a suppression of the second term related to track 2 by setting $w_2 \approx 0$, and keeping w_1 unchanged, in the total output signal $\Delta V = w_1 N_{Pulse,1} + w_2 N_{Pulse,2}$. The Kerr image reproduced in Fig. 4h explains that in the latter case, the detected skyrmion number is close to zero in track 2.

Device scaling

The neuromorphic weighted sum device can be scaled to accommodate more inputs and outputs using a crossbar-array geometry (Fig. 5a). By adding more input tracks to a device like the one shown in Fig. 4, the system scales linearly; M parallel tracks can support a weighted sum of M inputs. To increase the number of outputs to L, additional notches and Hall bars can be introduced along the track. Utilizing high-resistivity electrodes for AHE measurements, such as Ta used in our study, can mitigate issues like current leaks and sneak paths that are common in traditional crossbar arrays with oxide materials and conductive electrodes. One advantage of our device, compared with previously proposed neuromorphic devices using skyrmions[19], is that it requires only one transistor per synapse, rather than two transistors per synapse, thereby reducing the device area and read energy.

To realize a neuromorphic computing device, a nonlinear activation function must be applied to the weighted sum results, which has not yet been investigated in the present work. Such a function can be applied to the resulting AHE voltage ΔV by leveraging CMOS technology[41], which is compatible with our device, or magnetic tunnel junctions (MTJs)[20,42]. In deep neural networks, multiply-and-accumulate operations are the most dominant and are, thus, crucial to be executed efficiently in hardware[43].

MTJs could also be used directly for electrical skyrmion detection through their TMR ratio instead of relying on linear Hall voltages. The device concept is schematically illustrated in Fig. 5a. A large TMR ratio, akin to those in magnetoresistive random access memory (MRAM) MTJ bits, could provide a more robust output signal, simplifying the on-chip detection circuits. The TMR signal is expected to monotonically increase with the cumulative number of skyrmions beneath the MTJ, and to introduce the necessary nonlinearity, especially for large TMR (Supplementary Note 8 and Supplementary Fig. 11). Consequently, using MTJs as skyrmion detectors can intrinsically apply the nonlinear activation function of the neurons directly at the crossbar outputs. This approach has the potential to execute all the essential neuromorphic computing operations within a single device, eliminating the need for external electrical interconnections between the individual neural layer components.

In our demonstration, the input is coded by the current pulse number directed to a track, and the Hall voltage serves as the output signal. For the future integration of multiple crossbar arrays, consistent types of input and output would be beneficial. One approach is to use spin or orbital torques for skyrmion nucleation[44], rather than thermal effects. These torques should also result in a linear correlation between the current density and the number of skyrmions. Therefore, the amplitude of the current pulses could act as an input parameter. Conveniently, conversions between such inputs and outputs could be efficiently executed in CMOS using straightforward amplification with transistors. Another promising direction involves utilizing voltage-controlled magnetic anisotropy (VCMA) to induce skyrmion nucleation by applying a gate voltage within the nucleation sites[16,17,45,46]. In this scenario, the inputs are directly encoded in voltage amplitudes, ensuring direct consistency with the output voltages.

Tunable weights

Our experimental proof-of-concept device features fixed weights, but we demonstrate that they can be tuned by modifying the local magnetic fields at the nucleation sites. A viable approach for developing miniature trainable devices involves leveraging magneto-ionic effects. By applying electric-field gating, these effects can induce local, non-volatile and reversible alterations to the magnetic anisotropy and Dzyaloshinskii–Moriya interaction within the magnetic multilayer stack[47–50]. Such modifications enable the tuning of skyrmion

nucleation[45,46] and dynamics[51,52], effectively adjusting the synaptic weights, in a non-volatile and reversible way[49,53]. We recently showed the ability to control the magnetic properties and the domain pattern in multirepeat Pt/Co/Al multilayers similar to those used in this work[54]. Moreover, the observed linear correlation between the number of nucleated skyrmions and the OOP external magnetic field (Fig. 2h) strongly suggests a potential linear relationship between the number of nucleated skyrmions and the sample's anisotropy field. This could lead to a straightforward calibration of the synaptic weights. The gate used for the magneto-ionic modification of magnetic properties could also be used for VCMA-induced skyrmion nucleation with reduced energy requirements[16,17,45,46]. This could be achieved by leveraging different timescales for the VCMA nucleation of skyrmions. Figure 5a shows a schematic of the nucleation site design for VCMA-based nucleation and weight control.

Another approach for implementing non-volatile weights involves harnessing skyrmion non-volatility to avoid the nucleation step at every computational iteration. Input current pulses would be used exclusively to move skyrmions from the initial nucleation site towards the detection zone, with a number of skyrmions reaching this area that needs to be proportional to the current pulse input. Then, the skyrmions would be moved back to the nucleation site by electric pulses of opposite polarity. By adjusting the total number of skyrmions within the track at the nucleation site, non-volatile weights can be effectively realized. However, a reversible skyrmion motion is required to prevent alteration of the effective weight.

Energy of synaptic operation

The energy for our proposed skyrmionic weighted sum is determined by the nucleation energy of a skyrmion. We experimentally demonstrate this sum operation using a thermal nucleation scheme[6], related to a temperature increase by about $\Delta T \approx 100$ K, leading to $E_{th} \approx 10$ pJ per skyrmion (Supplementary Note 9). Reducing the metallic volume to be heated can further decrease E_{th} to the picojoule per skyrmion range. In our experimental device, the heat energy is provided by a current pulse and has been estimated to be approximately 20 pJ per skyrmion (Supplementary Note 9), corresponding well to the expected thermal energy required for the nucleation of a skyrmion. In practical devices in which skyrmion counting via Kerr microscopy would be unnecessary, reducing their size decreases the energy consumption and increases compactness with the square of the diameter: for 30-nm-diameter skyrmions, we expect a 50-fold reduction. Skyrmions can be scaled down to diameters as small as a few tens of nanometres in magnetic multilayers at room temperature[8,55], and there is no strict physical limitation to decrease them further to the scale of a few nanometres.

Efficient nucleation techniques, such as VCMA, can potentially lower the nucleation energy to just under 100 fJ, based on recent MTJ experiments[16,17]. VCMA devices, given their input and weight encoding, promise substantial energy savings per synaptic event compared with neuromorphic CMOS chips (~10 pJ per synaptic event[30]), with the added benefit of weight retention. This is close to the energy consumption of a biological synaptic event, approximately ~25 fJ, associated with vesicle release[31], underscoring the potential of skyrmions for brain-equivalent efficiency in neuromorphic computing. Although stochastic thermal nucleation is used in this work, deterministic generation is suitable as the only requirement is linearity. VCMA nucleation could avoid the requirement of skyrmion motion between nucleation and detection sites by directly nucleating the skyrmions through voltage within an MTJ[16,17]. This nucleation method also mitigates the adverse effects of thermal fluctuations in our system, which might otherwise affect the motion of skyrmions, including the skyrmion Hall angle[37,56,57]. Additionally, skyrmions can also be annihilated by a gate voltage in MTJs, offering an electrical reset method when MTJs are used[16]. Finally, the lowest energy for skyrmion nucleation that can be expected is approximately $500 k_B T \approx 2$ aJ at $T = 300$ K, corresponding to the energy barrier to stabilize skyrmions.

In addition to the skyrmion nucleation energy contribution, the comprehensive evaluation of energy consumption in the device necessitates the consideration of supplementary factors, including the energy expended during the electrical readout and reset of the skyrmion number and the operation of the CMOS circuit. However, the exhaustive estimation and optimization of these energy components lie beyond the scope of this study. The readout energy may be reduced by the utilization of optimized MTJs with a substantial TMR ratio, coupled with operation at high frequencies, which could lead to values below femtojoules[58]. It should also be emphasized that these improvements will be highly challenging to achieve, with several cross-compatibility issues and necessary compromises between the proposed improvement solutions. For instance, combining nucleation and detection sites at the same location requires the development of gate materials that simultaneously provide a large TMR signal, non-volatile magnetic property changes via magneto-ionic gating and VCMA skyrmion nucleation, presenting a material challenge due to the competing requirements of these functionalities. In the case of separated nucleation and detection sites, development is required to facilitate the displacement of skyrmions from one site to the other. In particular, the processes of nucleation at one MTJ and displacement and detection at a separate MTJ have already been demonstrated for domain walls[59].

Reliability of the sum operation

The thermal origin of skyrmion nucleation makes the process stochastic. If the system is tuned to produce one skyrmion per electrical pulse, the outcome can be different than the one with probability $p(\bar{1})$. In our experimental devices, we observe the nucleation of zero, one or two skyrmions when the current pulses are shaped to create a single skyrmion per pulse on average. We have performed numerical simulations for several values of $p(1)$ to determine the relative deviation σ of the number of nucleated skyrmions N_{Sk} for N_{Pulse} electrical pulses (Supplementary Note 10). Assuming that $p(0) = p(2) = p(\bar{1})/2$, the results show an excellent agreement with the formula $\sigma \approx \sqrt{p(\bar{1})/N_{Pulse}}$ (Fig. 5b). In our prototype, we estimate $p(1)$ to be approximately 0.6, a number that also accounts for the detection noise (Supplementary Note 10). This number is comparable with the probability of vesicle release in biology (corresponding to the skyrmion nucleation in our concept) typically between 0.25 and 0.5 (ref. 32).

The precision of the sum operation is set by this nucleation probability. When M independent synapses with each one producing $N_{Sk,m}$, the expected standard deviation of the sum, $\sqrt{\Sigma_{m=1}^{M}\sigma^2(m)}$, is equal to $\sqrt{M}\sigma$ if all the synapses have the same standard deviation. When N_{Pulse} pulses are injected per synapse, the sum is equal to MN_{Pulse}, the precision of the sum is given by $1 - \sigma(N_{Pulse})/\sqrt{M} = 1 - \sqrt{p(\bar{1})/(MN_{Pulse})}$ and the mean energy cost is MN_{Pulse} times the estimated skyrmion nucleation energy. In Fig. 5c, we show the relationship between the sum precision and the mean energy cost for ten synaptic operations ($M = 10$). Achieving a higher precision necessitates greater energy consumption. Consequently, an optimal operating point can be identified by balancing the energy cost against the sum precision requirements, akin to a trade-off encountered in biology[32]. As shown in Fig. 5c, a relatively high precision on the sum operation can be achieved at a low energy cost, even when using $p(1) \approx 0.6$. Additionally, deep neural network architectures can be robust against local inaccuracies, which can be absorbed by the network. Two alternative paths for device optimization are (1) to encode numbers with larger number of skyrmions or (2) to improve the deterministic nucleation of skyrmions. Other nucleation schemes, for example, inspired by MRAM technologies, might reduce $p(\bar{1})$ by many orders of magnitude. For 10 synaptic operations, the lowest physical limit for the energy required for skyrmion nucleation is in the range of 10 aJ to 1 fJ, and a single synaptic operation is in the 1–100 aJ range.

Conclusions

We have reported a neuromorphic weighted sum based on magnetic skyrmions. We first developed a method for electrically controlling skyrmion nucleation and movement within specially crafted magnetic multilayered tracks. The linear association between the number of generated skyrmions and applied current pulses, under various sets of parameters, implements the multiplication of inputs by a synaptic weight. The weight can be finely tuned through minor adjustments to the OOP external magnetic field (close to −0.57 skyrmions per pulse and per mT). Using optimized parameters, we demonstrated the injection of over 50 skyrmions into a 6-µm-wide track.

Our design uses highly resistive Ta-based transverse electrodes connected only to the edge of the track, enabling the electrical detection of skyrmions via the AHE without adversely affecting their motion or providing sneak paths in crossbar arrays. We validated the weighted sum operation in a device featuring two parallel tracks intersected by a Hall electrode; the resulting Hall voltage corresponds to the combined number of skyrmions in both tracks. This ensures the efficient execution of the fundamental weighted sum operation, a cornerstone for neuromorphic computing.

Looking forward, integrating magneto-ionic effects for non-volatile, reversible control over local magnetic properties, along with nonlinear electrical detection via MTJs, could provide comprehensive functionality for neuromorphic computing. The approach could, ultimately, lead to brain-inspired hardware capable of weighted sums at an energy expenditure as minimal as 1–100 aJ per synaptic operation.

Methods

Device fabrication

The multilayered stack used to stabilize skyrmions at room temperature is Ta(5 nm)/Pt(8 nm)/[Co(1.2 nm)/Al(3 nm)/Pt(3 nm)]$_{10}$, with the index '10' signifying ten repetitions of the trilayer, and this stack is grown at room temperature by magnetron sputtering on Si_3N_4 substrates. This multilayer stack leverages both interfacial Dzyaloshinskii–Moriya interaction and perpendicular magnetic anisotropy, allowing to stabilize skyrmions of approximately 200 nm in diameter at room temperature. The Si_3N_4 substrates are used to enhance thermal energy dissipation and minimize the number of nucleated skyrmions in our demonstrative device, allowing for easy visual counting and enhancing the visual observation of the device operation. The device geometries are defined by a three-step ultraviolet lithography process. The first step is used to define the track geometry (Fig. 1d, green), as well as contacts for the Hall electrodes, which is obtained by Ar^+-ion etching of the multilayer film. The track shown in green in the Kerr microscopy images (Fig. 2a–d) spans 6 µm in width and 40 µm in length, bearing an impedance of 98 Ω including the contacts. It incorporates a rounded triangular nucleation notch, accounting for roughly 17% of the track's width. The second step is used to define the crossing Hall bar electrodes (Fig. 1d, red), still by ultraviolet lithography, and keeping the resist mask used for the first step to ensure that the electrodes are only connected on the edge of the multilayer track. Then, 10-nm-thick Ta electrodes are deposited by sputtering and lifted-off, measuring 3 µm in width for the devices shown in Figs. 2 and 3. Finally, the third lithography step is used to lift-off the sputtered Ti (10 nm)/Au (200 nm) electrical contacts for electrical measurements. The proof-of-concept device used to demonstrate the weighted sum operation (Fig. 4a) consists of two parallel magnetic multilayered tracks, each 6 µm wide and equipped with a nucleation notch. These tracks are intersected by a 6-µm-wide Ta Hall electrode.

Kerr microscopy

Kerr microscopy is used to observe and count the skyrmions in the devices. For each measurement series, a reference image is taken in the saturation state and subtracted from the displayed image. This image difference enhances the magnetic contrast, and reduces the 'topographical' features. The light source is a blue light-emitting diode (LED) with a peak intensity at 445 nm wavelength. For the maximum resolution, we use a ×100 lens in immersion in a high-refractive-index oil (n = 1.5) and large numerical aperture (1.3). Due to thermal drifts, the sample is realigned before each image using a three-dimensional piezoelectric stage. The focus is a key parameter to get the contrast of the sub-wavelength-diameter skyrmions. A fine-focus series of images is taken by varying the focus to achieve the maximum resolution. The best-focused image is automatically selected, and its optimized focus position is then forwarded for the next image acquisition. Due to this procedure, each acquisition typically takes a few minutes. A final fine correction for the drift in planar directions is made in post-treatment.

The colours of the Kerr images presented in this work have been modified to improve the readability of the figures; Kerr images without colour modifications are provided in Supplementary Note 11.

Electrical measurements

Skyrmions are nucleated and moved using pulses generated by an arbitrary waveform generator connected to a 38 dB amplifier, with typical voltages in the range of volts. The Hall voltage measurements are performed by using a d.c. current source and a nanovoltmeter to measure the transverse Hall voltage with a current of 100 µA. This current corresponds to a current density in the range of 0.1 GA m^{-2}, which is about three orders of magnitude below the threshold current for skyrmion nucleation and motion. To improve the electrical measurement precision, each voltage measurement is the average of 50 individual pair of measurements with positive and negative currents of 100 µA with a duration of 100 ms. The measured transverse voltage is considered to be proportional to the mean magnetization along the z direction[13]. AHE loop measurements are obtained by sweeping an OOP external magnetic field and recording the Hall voltage to which an offset is subtracted. The offset corresponds to a small longitudinal voltage component (Supplementary Note 2 and Supplementary Fig. 3).

The measurement sequence for building the block device shown in Fig. 3 is as follows. Initially, ten voltage measurements are taken without any skyrmion injections to determine the saturated magnetization value, that is, when no skyrmions are present. In the depicted graph, these ten initial data points exhibit a consistent Hall voltage, with $\Delta V \approx 0$. Following this, 20 current pulses are used to nucleate skyrmions. After each pulse, both Hall voltage and Kerr image are recorded. To conclude the measurement sequence, a saturating field of 200 mT is applied and ten voltage measurements are again performed at saturation to correct for voltage drifts.

For the measurements of a single device composed of parallel multilayer tracks, the tracks are connected in parallel to a d.c. current source. Tracks 1 and 2 have a resistance value of 130 Ω and 120 Ω, respectively. Each track has calibrated resistances of 12 kΩ in series at each end of each track. This ensures an identical (within 0.1%) d.c. current of 100 µA flowing in each track. Moreover, it guarantees that the voltage measured at the edge of the Hall cross only arises from the device instead of the electrical circuit used for the measurement (Supplementary Note 7; Supplementary Fig. 10a shows a schematic of the electrical circuit). With this circuit, the Hall voltage measurement is indeed found to be the sum of the individual Hall voltage of each individual track (Supplementary Note 7 and Supplementary Fig. 10b). This indicates that the Hall voltage measured at the edge of the device accounts for the sum of the magnetization contribution of the two Hall crosses. Bias tees are used to selectively inject current pulses or d.c. current within the desired track. The measurement sequence for the prototype device (Fig. 4) is the same as for the individual track, that is, 20 measurements of the Hall voltage are taken after fully saturating the tracks' magnetization and a Kerr image is taken as the reference. Then, 20 pulses are applied to track 1, each pulse being followed by a voltage measurement, whereas Kerr images are taken after every 5 pulses. Then, 20 more voltage measurements are carried out to check

the voltage stability. The same process is then repeated for track 2. Finally, a saturating field of 200 mT is applied and 10 voltage measurements are taken.

The quoted current densities are the averaged ones estimated by dividing the total current by the width of the track (6 µm) and the total magnetic multilayer thickness (85 nm).

Data availability

The data that support the findings of this study are available via Zenodo at https://doi.org/10.5281/zenodo.13988409 (ref. 60). Other relevant data are available from the corresponding authors on request.

References

1. Fert, A., Reyren, N. & Cros, V. Magnetic skyrmions: advances in physics and potential applications. *Nat. Rev. Mater.* **2**, 17031 (2017).
2. Moreau-Luchaire, C. et al. Additive interfacial chiral interaction in multilayers for stabilization of small individual skyrmions at room temperature. *Nat. Nanotechnol.* **11**, 444–448 (2016).
3. Jiang, W. et al. Blowing magnetic skyrmion bubbles. *Science* **349**, 283–286 (2015).
4. Woo, S. et al. Observation of room-temperature magnetic skyrmions and their current-driven dynamics in ultrathin metallic ferromagnets. *Nat. Mater.* **15**, 501–506 (2016).
5. Boulle, O. et al. Room-temperature chiral magnetic skyrmions in ultrathin magnetic nanostructures. *Nat. Nanotechnol.* **11**, 449–454 (2016).
6. Legrand, W. et al. Room-temperature current-induced generation and motion of sub-100 nm skyrmions. *Nano Lett.* **17**, 2703–2712 (2017).
7. Büttner, F. et al. Field-free deterministic ultrafast creation of magnetic skyrmions by spin–orbit torques. *Nat. Nanotechnol.* **12**, 1040–1044 (2017).
8. Soumyanarayanan, A. et al. Tunable room-temperature magnetic skyrmions in Ir/Fe/Co/Pt multilayers. *Nat. Mater.* **16**, 898–904 (2017).
9. Finizio, S. et al. Deterministic field-free skyrmion nucleation at a nanoengineered injector device. *Nano Lett.* **19**, 7246–7255 (2019).
10. Wang, Z. et al. Thermal generation, manipulation and thermoelectric detection of skyrmions. *Nat. Electron.* **3**, 672–679 (2020).
11. Woo, S. et al. Deterministic creation and deletion of a single magnetic skyrmion observed by direct time-resolved X-ray microscopy. *Nat. Electron.* **1**, 288–296 (2018).
12. Yang, S. et al. Electrical generation and deletion of magnetic skyrmion-bubbles via vertical current injection. *Adv. Mater.* **33**, 2104406 (2021).
13. Maccariello, D. et al. Electrical detection of single magnetic skyrmions in metallic multilayers at room temperature. *Nat. Nanotechnol.* **13**, 233–237 (2018).
14. Zeissler, K. et al. Discrete Hall resistivity contribution from Néel skyrmions in multilayer nanodiscs. *Nat. Nanotechnol.* **13**, 1161–1166 (2018).
15. Hanneken, C. et al. Electrical detection of magnetic skyrmions by tunnelling non-collinear magnetoresistance. *Nat. Nanotechnol.* **10**, 1039–1042 (2015).
16. Chen, S. et al. All-electrical skyrmionic magnetic tunnel junction. *Nature* **627**, 522–527 (2024).
17. Urrestarazu Larrañaga, J. et al. Electrical detection and nucleation of a magnetic skyrmion in a magnetic tunnel junction observed via operando magnetic microscopy. *Nano Lett.* **24**, 3557–3565 (2024).
18. Bourianoff, G., Pinna, D., Sitte, M. & Everschor-Sitte, K. Potential implementation of reservoir computing models based on magnetic skyrmions. *AIP Adv.* **8**, 055602 (2018).
19. Song, K. M. et al. Skyrmion-based artificial synapses for neuromorphic computing. *Nat. Electron.* **3**, 148–155 (2020).
20. Grollier, J. et al. Neuromorphic spintronics. *Nat. Electron.* **3**, 360–370 (2020).
21. Huang, Y., Kang, W., Zhang, X., Zhou, Y. & Zhao, W. Magnetic skyrmion-based synaptic devices. *Nanotechnology* **28**, 08LT02 (2017).
22. Sharad, M., Augustine, C., Panagopoulos, G. & Roy, K. Spin-based neuron model with domain-wall magnets as synapse. *IEEE Trans. Nanotechnol.* **11**, 843–853 (2012).
23. Chen, R. et al. Nanoscale room-temperature multilayer skyrmionic synapse for deep spiking neural networks. *Phys. Rev. Appl.* **14**, 014096 (2020).
24. Pinna, D. et al. Skyrmion gas manipulation for probabilistic computing. *Phys. Rev. Appl.* **9**, 064018 (2018).
25. Zázvorka, J. et al. Thermal skyrmion diffusion used in a reshuffler device. *Nat. Nanotechnol.* **14**, 658–661 (2019).
26. Prychynenko, D. et al. Magnetic skyrmion as a nonlinear resistive element: a potential building block for reservoir computing. *Phys. Rev. Appl.* **9**, 014034 (2018).
27. Raab, K. et al. Brownian reservoir computing realized using geometrically confined skyrmion dynamics. *Nat. Commun.* **13**, 6982 (2022).
28. Yokouchi, T. et al. Pattern recognition with neuromorphic computing using magnetic field–induced dynamics of skyrmions. *Sci. Adv.* **8**, eabq5652 (2023).
29. Sun, Y. et al. Experimental demonstration of a skyrmion-enhanced strain-mediated physical reservoir computing system. *Nat. Commun.* **14**, 3434 (2023).
30. Frenkel, C., Lefebvre, M., Legat, J.-D. & Bol, D. A 0.086-mm^2 12.7-pJ/SOP 64k-synapse 256-neuron online-learning digital spiking neuromorphic processor in 28-nm CMOS. *IEEE Trans. Biomed. Circuits Syst.* **13**, 145–158 (2019).
31. Attwell, D. & Laughlin, S. B. An energy budget for signaling in the grey matter of the brain. *J. Cerebr. Blood Flow Metab.* **21**, 1133–1145 (2001).
32. Harris, J. J., Jolivet, R. & Attwell, D. Synaptic energy use and supply. *Neuron* **75**, 762–777 (2012).
33. Chanaday, N. L., Cousin, M. A., Milosevic, I., Watanabe, S. & Morgan, J. R. The synaptic vesicle cycle revisited: new insights into the modes and mechanisms. *J. Neurosci.* **39**, 8209–8216 (2019).
34. Kent, N. et al. Creation and observation of hopfions in magnetic multilayer systems. *Nat. Commun.* **12**, 1562 (2021).
35. Grelier, M. et al. Three-dimensional skyrmionic cocoons in magnetic multilayers. *Nat. Commun.* **13**, 6843 (2022).
36. Krishnia, S. et al. Large interfacial Rashba interaction generating strong spin–orbit torques in atomically thin metallic heterostructures. *Nano Lett.* **23**, 6785–6791 (2023).
37. Jiang, W. et al. Direct observation of the skyrmion Hall effect. *Nat. Phys.* **13**, 162–169 (2017).
38. Fert, A., Cros, V. & Sampaio, J. Skyrmions on the track. *Nat. Nanotechnol.* **8**, 152–156 (2013).
39. He, B. et al. All-electrical 9-bit skyrmion-based racetrack memory designed with laser irradiation. *Nano Lett.* **23**, 9482–9490 (2023).
40. Figueiredo-Prestes, N. et al. Magnetization switching and deterministic nucleation in Co/Ni multilayered disks induced by spin-orbit torques. *Appl. Phys. Lett.* **119**, 032410 (2021).
41. Ambrogio, S. et al. An analog-AI chip for energy-efficient speech recognition and transcription. *Nature* **620**, 768–775 (2023).
42. Torrejon, J. et al. Neuromorphic computing with nanoscale spintronic oscillators. *Nature* **547**, 428–431 (2017).
43. Azghadi, M. R. et al. Hardware implementation of deep network accelerators towards healthcare and biomedical applications. *IEEE Trans. Biomed. Circuits Syst.* **14**, 1138–1159 (2020).

44. Krishnia, S. et al. Quantifying the large contribution from orbital Rashba-Edelstein effect to the effective damping-like torque on magnetization. *APL Mater.* **12**, 051105 (2024).
45. Schott, M. et al. The skyrmion switch: turning magnetic skyrmion bubbles on and off with an electric field. *Nano Lett.* **17**, 3006–3012 (2017).
46. Bhattacharya, D. et al. Creation and annihilation of non-volatile fixed magnetic skyrmions using voltage control of magnetic anisotropy. *Nat. Electron.* **3**, 539–545 (2020).
47. Bernand-Mantel, A. et al. Electric-field control of domain wall nucleation and pinning in a metallic ferromagnet. *Appl. Phys. Lett.* **102**, 122406 (2013).
48. Bauer, U. et al. Magneto-ionic control of interfacial magnetism. *Nat. Mater.* **14**, 174–181 (2015).
49. Herrera Diez, L. et al. Nonvolatile ionic modification of the Dzyaloshinskii-Moriya interaction. *Phys. Rev. Appl.* **12**, 034005 (2019).
50. Srivastava, T. et al. Large-voltage tuning of Dzyaloshinskii–Moriya interactions: a route toward dynamic control of skyrmion chirality. *Nano Lett.* **18**, 4871–4877 (2018).
51. Fillion, C.-E. et al. Gate-controlled skyrmion and domain wall chirality. *Nat. Commun.* **13**, 5257 (2022).
52. Dai, B. et al. Electric field manipulation of spin chirality and skyrmion dynamic. *Sci. Adv.* **9**, eade6836 (2023).
53. Mishra, R., Kumar, D. & Yang, H. Oxygen-migration-based spintronic device emulating a biological synapse. *Phys. Rev. Appl.* **11**, 054065 (2019).
54. da Câmara Santa Clara Gomes, T. et al. Control of the magnetic anisotropy in multirepeat Pt/Co/Al heterostructures using magnetoionic gating. *Phys. Rev. Appl.* **21**, 024010 (2024).
55. Legrand, W. et al. Room-temperature stabilization of antiferromagnetic skyrmions in synthetic antiferromagnets. *Nat. Mater.* **19**, 34–42 (2020).
56. Juge, R. et al. Current-driven skyrmion dynamics and drive-dependent skyrmion Hall effect in an ultrathin film. *Phys. Rev. Appl.* **12**, 044007 (2019).
57. Litzius, K. et al. The role of temperature and drive current in skyrmion dynamics. *Nat. Electron.* **3**, 30–36 (2020).
58. He, Z. & Fan, D. A tunable magnetic skyrmion neuron cluster for energy efficient artificial neural network. In *Design, Automation & Test in Europe Conference & Exhibition (DATE) 2017* 350–355 (IEEE, 2017).
59. Raymenants, E. et al. Nanoscale domain wall devices with magnetic tunnel junction read and write. *Nat. Electron.* **4**, 392–398 (2021).
60. da Câmara Santa Clara Gomes, T. et al. Data for: Neuromorphic weighted sums with magnetic skyrmions. *Zenodo* https://doi.org/10.5281/zenodo.13988409 (2024).

Acknowledgements

This work is supported by the Horizon 2020 Framework Program of the European Commission under FET-Proactive Grant SKYTOP (no. 824123), by the European Research Council advanced grant GrenaDyn (reference no. 101020684), by the EU project SkyANN (reference no. 101135729) and from a France 2030 government grant managed by the French National Research Agency (grant no. ANR-22-EXSP-0002 PEPR SPIN CHIREX).

Author contributions

M.-B.M., P.S., V.C., J.G. and N.R. conceived the project. N.R., D.S.-H., Y.S. and T.d.C.S.C.G. designed the measurement procedure. S.C., Y.S. and T.d.C.S.C.G. grew the multilayer films and Ta electrodes. T.d.C.S.C.G. patterned the samples, acquired the magneto-optic Kerr effect and transport data, treated and analysed the data with support from Y.S., D.S.-H., S.K., M.-B.M., P.S., V.C., J.G. and N.R. T.d.C.S.C.G., V.C., J.G. and N.R. prepared the manuscript. All authors discussed and commented on the manuscript.

Competing interests

The authors declare no competing interests.

Additional information

Supplementary information The online version contains supplementary material available at https://doi.org/10.1038/s41928-024-01303-z.

Correspondence and requests for materials should be addressed to Tristan da Câmara Santa Clara Gomes, Vincent Cros, Julie Grollier or Nicolas Reyren.

Peer review information *Nature Electronics* thanks Jayasimha Atulasimha and the other, anonymous, reviewer(s) for their contribution to the peer review of this work.